X-Ray Diffraction of Ramp Compressed Solid Silicon to 390 GPa

X. Gong, D. N. Polsin, R. Paul, B. J. Henderson, J. R. Rygg,
J. H. Eggert, A. Lazicki, F. Coppari, R. Smith, G. W. Collins
Laboratory for Laser Energetics, University of Rochester, Rochester, New York 14623-1299, USA
(Dated: March 2, 2021)

Silicon was ramp-compressed along a low-temperature thermodynamic path to final stress states between 33 and 390 GPa using OMEGA-EP laser. Nanosecond in-situ x-ray diffraction shows a hexagonal close-packed (hcp) crystal structure at 33 GPa persists to 100 GPa, and by 150 GPa silicon transitions to the face-centered-cubic (fcc) structure which persists to 390 GPa, the highest pressure studied. No evidence is seen for a theoretically-predicted double hexagonal closed-packed (dhcp) structure in the vicinity of 40 GPa along the thermodynamic path followed in the experiments. We also used gray body emission and hydrodynamic simulations to estimate the temperature at the achieved thermodynamic states.

INTRODUCTION

[The first paragraph should not emphasize the theoretical results and difficulty of experimentally measuring XRD on Si in the multi-TPa range. Instead, focus the first paragraph on the interest and relevance of Si, including some of the interesting behavior seen in DAC and shock studies at lower pressure. Then, in the second paragraph you can dig into the previous data a bit more, and also discuss the theoretical predictions in the region that you have studied (theory possibly in a 3rd paragraph, as you show). Then, in the final paragraph of your introduction, give a brief outline of what is discussed in the paper, and include the key results.]

Silicon, being one of the most abundant elements in nature, has been studied extensively at ambient conditions, and at higher pressure under quasi-static compression. Experimental studies reveal several solid phases at ambient temperature (300 K), as summarized in Table I. The existence of these solid phases has been studied theoretically, using first-principle calculations, and has been confirmed experimentally [1].

Knowledge of silicon at thermodynamic states away from the 300 K isotherm is also desired due to importance to Inertial Confinement Fusion (ICF)[2], among others. Shock compression experiments, being able to access very high-pressure and high-temperature states, have been used extensively for examining material phase diagrams that are not accessible using static compression techniques [3][4][5][6][7]. The phases near the melt curve of Si has been studied using *in-situ* x-ray diffraction under shock compression recently. The results are quite consistent with theory [1]. In [6], shock melting was unambiguously established above 31–33 GPa, and reshock from the melt boundary below 54 GPa results in recrystallization to the hcp Si phase. In [7], a shock-induced lowering of the onset of phase transitions is demonstrated. These studies reveal a quite complicated phase diagram of solid Si.

Theoretical calculation reveals a double hexagonal close packed (dhcp) phase at pressure range 33–41 GPa at room temperature [8]. This however contradicts the previously stated experimental results because no such phase is observed at room temperature. On the other hand, [1] predicts the existence of dhcp phase at similar pressure range, but between 400 K and melt curve. This region of the phase diagram can be easily accessed through ramp compression [9][10][11], which comprises a series of weak shocks. If the compression is gentle enough such that it can been viewed as an infinite number of infinitesimal shocks, the compression can be considered isentropic. In general, ramp compression allows a relatively cool thermodynamic compression path to be followed. In this way materials can stay in the solid phase to much higher pressures and achieve higher compression states.

In this work, we study the existence of the predicted Si dhcp phase and the structure of Si at pressures as high as possibly achievable of ramp-compressed Si, by combining in-situ x-ray diffraction and velocimetry techniques.

EXPERIMENTAL METHOD

Experiments were performed on the OMEGA EP laser at the University of Rochester, Laboratory for Laser Energetics. The experimental configuration is shown in Fig.(1). The hardware is "Powder X-Ray Diffraction Image Plates" or "PXRDIP" [9] in short, consisting of a $50 \times 50 \times 75\,\mathrm{mm}^3$ rectangular box with a $10 \times 10\,\mathrm{mm}^2$ cavity on the front square face where the target package is mounted, and a 25 mm diameter circular aperture on the back face through which the VISAR probe beam can pass. Four rectangular image plates of $50 \times 75\,\mathrm{mm}^2$ are used to record x-rays.

The silicon sample is ⟨100⟩-oriented, single crystal, 20-µm-thick, cut from a waffle, and is sandwiched between plates of ⟨110⟩-oriented, single crystal, 20-µm-thick diamond ablator, and ⟨100⟩-oriented, single crystal, 100-µm-thick lithium fluoride (LiF) window. The stack is mounted on a 75-µm thick tungsten, tantalum or platinum plate with a 300-µm-diameter pinhole aperture.

Compression is accomplished by ablating the diamond

TABLE I: Silicon phases at ambient temperature and 800 K [1]

Index	Phase	Pressure (GPa) @ 300 K (Experiment)	Pressure (GPa) @ 800 K (Theory)
Si-I	cubic-diamond (cd)	0 – 12.5	0 – 11.2
Si-II	β-tin	8.8 – 16	11.2 – 11.7
Si-XI	body-centered orthorhombic *Imma*	13 – 16	11.7 – 13.9
Si-V	simple hexagonal (sh)	14 – 38	13.9 – 21.4
Si-VI	*Cmce*	40 – 42	21.4 – 24.2
?	dhcp	Does not exist	24.2 – 53.7
Si-VII	hexagonal close packed (hcp)	40 – 78	53.7 – 60.8
Si-X	face-centered cubic (fcc)	78 – 248	60.8 – 2827.1

ablator with a laser pulse with gradually increasing power over 10 ns, creating a rapidly expanding plasma and generating a compression wave with gradually increasing intensity that propagates into the diamond. The compression wave reverberates between diamond and LiF layer, effectively compressing the silicon sample to high pressure through large number of weak shocks, keeping its temperature relatively low. The laser beam has an incident angle of 22.5° with respect to the target normal and a 1100-µm spot size with a super-Gaussian profile produced by distributed phase plates.

The x-ray used for diffraction is produced by illuminating a back-lighter foil (such as Cu and Ge) with an 1-ns laser beam with square pulse shape. The intensity is chosen to optimize x-ray conversion efficiency of Cu He-α (8.38 keV or 1.481 Å) and Ge He-α (19.25 keV or 1.210 Å)[12]. The x-ray timing is chosen to coincide with peak compression of the silicon sample.

ANALYSIS AND RESULTS

Pressure determination

The pressure within the Si sample is indirectly inferred from the measured Si-LiF interface velocity using the method of characteristics [13]. According to the theory of isentropic flow, Riemann in-variants $J_\pm = u_p \pm \int dP/\rho_0 c_L$ are conserved along characteristics $C_\pm$: $dh/dt = \pm c_L$, where u_p is particle velocity, ρ_0 is ambient density, c_L is Lagrangian sound speed, and h is Lagrangian coordinate. With the knowledge of the mechanical response of LiF under ramp compression $P = P(u_p)$, the Si-LiF interface pressure can be deduced. The boundary conditions at the Si-LiF interface $u_p(t)$, $P(t)$ and $c_L(t)$ form the Riemann in-variants $J_\pm(t)$ and they are back-propagated into the Si-sample along characteristics, determined by the local sound speed, which can in turn be solved from the local Riemann in-variants. This process effectively produces a pressure map in the Si sample as a function of space and time. The pressure within the Si sample during the x-ray exposure is of course non-uniform and non-steady.

The pressure determination process for OMEGA EP shot 29627 is outlined in Figure 2 as an example. The Si-LiF interface velocity is measured as a function of time using VISAR [14]. This velocity is mapped onto the interface pressure using LiF isentrope [15]. The pressure is back-propagated along characteristics in Si determined by the Si isentrope provided by the author of [1] (though the isentrope itself is not published), which produces inside the Si layer a 2-D pressure map as a function of Lagrangian position and time. The average pressure $\langle P \rangle$ and its spread (or dispersion) Δ_P during the x-ray exposure; in this case they are 185 GPa and 12 GPa respectively.

It should be stressed that the pressure in the Si sample is mostly dependent on the mechanical response of LiF rather than that of its own. This is due to primarily the jump condition at the Si-LiF interface, which requires that the particle velocity as well as pressure are continuous across the interface. Therefore the mechanical response of LiF together with measured interface velocity determines the pressure on both sides of the interface. It is expected that using different EOS of Si does not impact the pressure measurement of Si much, which is advantageous in this case because theoretically calculated EOS can vary depending on which exchange-correlation functional is used.

Pressure uncertainty is estimated using a Monte-Carlo algorithm. Random numbers are generated to produce velocity [14], x-ray timing, LiF refractive index [15], LiF mechanical response [15], and target thickness around their nominal values, and the pressure determination procedure is run to calculate $\langle P \rangle$ and Δ_P under these conditions. A large number of runs give a pool of pressure and pressure spread. Pressure uncertainty σ_P is the standard deviation of the pressure pool and is shown as the errorbar of larger capsize in Figure 5. We also include the average Δ_P, shown as the errorbar of smaller capsize in Figure 5, as a indicator of non-uniformity of pressure during x-ray exposure.

The validity of the method of characteristics may be challenged due to the existence of multi-wave structures, as is shown in Figure 2, for example, at 5 ns, 10 ns. These multi-wave structures arise from the material strength as well as the phase transition of Si at low pressures [3][6][7], leading to deviations from the ideal shockless

compression path. The analysis in [16] shows that, the existence of multiple shocks in the compression path does not alter $P(u_p)$ relation significantly. These shocks make the $c_L(u_p)$ relation more "rectangular" and very different from the smooth curve without the multiple shocks, but the pressure which is proportional to the area under this curve ($P = \rho_0 \int c_L(u_p) du_p$) has been shown to be different from an isentrope only up to third order in density. Therefore the method of characteristics can be safely used to infer pressures.

Phase Determination

X-rays scattered by lattice planes with spacing d constructively interfere when the Bragg condition $\lambda = 2d \sin\theta$ is satisfied, where λ is the probe x-ray wavelength, θ is half of the scattering angle. For single crystal samples and mono-energetic x-rays, this condition is rarely satisfied. However, for a powdered sample which consists of crystal grains with random orientations, uniform cones of diffracted x-rays for each allowed lattice plane will be produced. The cones intersect with image plates, producing a series of rings with constant 2θ. The diffraction pattern allows us to constrain crystal structure and determine lattice parameters, and furthermore, mass density. The silicon sample is initially single crystal, with [100] normal to its surface and direction of compression. Under compression, silicon is observed to undergo single-crystal to powder-like transition, resulting in powder-like continuous diffraction signal in ϕ space. This transition is not complete, in that the diffraction intensity is not uniform across the azimuth, which means the crystal grains that comprise the powdered sample are not completely randomly oriented.

Two types of diffraction pattern are observed as pressure increases. At pressures range 33(3)–99(4) GPa, the diffraction pattern displays characteristics of hexagonal lattice. In the example of Figure 3, the experimental x-ray intensity lineout as a function of diffraction angle 2θ is displayed in the first panel. The tungsten pinhole diffraction signal is indicated by gray shades. The rest of the peaks are from compressed Si sample. The comparison with simulated diffraction signal of hcp, dhcp and sh structures is illustrated. The experimental lineout matches well with hcp structure, but does not match well with sh structure in general. The dhcp structure, predicted by theory, is another strong contender. We notice the absence of (103) peak across the entire 2π of azimuth. Theoretically (103) peak has a much higher intensity than (104) peak. However we can observe the (104) peak, albeit highly textured. This suggests strongly against the dhcp structure. The structure is therefore interpreted as hcp, with $a = 2.472(5)$ Å, $c = 4.202(9)$ Å. The c/a ratio is 1.699(7), which is slightly above the ideal value 1.633. At pressures higher than 152(5) GPa, the diffraction pattern can be attributed to fcc structure. In the example of Figure **??**(b), (111), (200) and (220) peaks from fcc structure are observed. There are no data between 99(4) and 152(5) GPa, so the phase boundary is determined only to the extent of this interval.

Phase Diagram

The ρ-P phase diagram is shown in Fig.5. Static-compression [17][18][19][20], shock-compression [3][7] and ramp-compression (from this work) data are displayed, with colors indicating structures, and markers compression method. Two different isentropes, calculated using PBE-GGA, PBEsol exchange-correlation (xc) functionals are also shown. It is clear that the PBEsol xc functional is overestimating the density, because for a given pressure, isothermal or static compression should yield the highest density possible. The author of [1] also provided an isentrope calculated using SCAN-L xc functional, but it is practically identical to the PBE-GGA one, so only PBE-GGA is shown explicitly.

[Discuss physical implication]

The T-P phase diagram is shown in Fig. 6. Our data is overlaid on top of the theoretically calculated phase diagram[1], with red circles indicating hcp phase and blue circles indicating fcc phase. Since our experiment does not measure temperature directly, we assume the compression is shockless therefore our data lie on the isentrope. Along the isentrope, silicon is predicted [1] to assume dhcp structure in the pressure range of 10-60 GPa. However, three data points from our work indicate that silicon actually assumes hcp structure in this pressure regime. At slightly higher pressures, where theory predicts fcc structure, we still observed hcp structure, up to 99(4) GPa. Our data supports the prediction that silicon remains fcc structure, up to around 390(11) GPa. We do not have any observation above that pressure.

CONCLUSIONS

There has been a large collection of x-ray diffraction data for isothermally compressed Si up to 249 GPa, and several measurements along the shock Hugoniot also exist. We expand our knowledge of Si phase diagram to thermodynamic states between the isotherm and the Hugoniot, along a ramp loading path. We have shown that the theoretically predicted dhcp phase either does not exist (it is hcp instead) or in a different region in the phase space than predicted. The hcp-fcc phase boundary is also different from the theory prediction. We confirm the fcc to be stable up to 390 GPa which is the highest pressure we achieved. The theoretically predicted bcc phase at 2.8 TPa is currently outside the scope of this work.

SUPPLEMENTARY MATERIAL

Features on the Image Plates

The image plates in a typical experiment consist of the following features: (1) the direct x-ray image, produced by the x-ray passing through the pinhole without diffraction; (2) reference calibration diffraction lines from pinhole materials; (3) Laue spots from single crystal diamond and LiF since the x-ray source is not perfectly mono-chromatic; (4) spatially broad and smoothly varying background originating from x-rays created in the ablation plasma; (5) actual diffraction lines from Si sample. A least-squares minimization routine with features (1) and (2) as input determines best-fit values for the experimental geometry including image plate, x-ray source and pinhole locations. Then the image plates are projected onto $2\theta - \phi$ space, where ϕ is the azimuthal angle around the axis $\theta = 0$. See Fig.(**??**) for an example. A non-linear peak clipping algorithm is used to subtract feature (4) from the image.

Temperature Estimation

Temperature of the silicon sample during peak compression is estimated by combining hydrodynamic simulations and optical pyrometry.

Temperature could be estimated using hydrodynamic simulation HYADES. The equation of state tables used are: SESAME 7834 for diamond, SESAME 3810 for silicon, and SESAME 7271v3 for lithium fluoride. The Steinberg-Guinan strength model [21] is enabled for diamond with parameters taken from [22]. HYADES is an one-dimensional simulation code while our experiments are performed in a three-dimensional world. Not all laser energy deposited into the sample is used to compress it along its normal direction (part of the energy drives the lateral motions). An energy scaling factor smaller than unity is therefore assigned in the simulations, and is adjusted so that the simulated Si-LiF interface velocity is as close to our observation as possible. The silicon EOS, SESAME 3810 differs significantly from the more recent results [1], and certainly the real world silicon, so a perfect match is impossible. The peak velocity and the general velocity profile near the velocity plateau is prioritized when adjusting the energy scaling factor. The mean value of temperature and its standard deviation is extracted from the simulation with optimal energy scaling factor.

Experimentally, Streaked Optical Pyrometer (SOP) is traditionally used in shock experiments to measure the emission of the shock front and infer the temperature assuming the shock front behaves like a gray body [23]. The minimum temperature required for SOP is typically 0.5 eV, beyond the temperatures of this work according to the simulations. Nevertheless, SOP images display an observable increase in signal level after $t = 0$ (when laser is turned on), as shown in Fig.7. The signal increase can be attributed to the rise of Si temperature at the Si-LiF interface, or the glue temperature, or the LiF temperature. We performed HYADES simulations for some shots, with additional glue layer between Si and LiF. An example is shown in (figure here) for shot 29637. It is observed that during peak compression, the temperature of LiF does not exceed 1500 K, the glue is roughly at 1500 K, and the Si temperature at the Si-LiF interface is between 3400 K and 3900 K. Therefore the SOP signal increase is attributed to Si temperature increase at the Si-LiF interface.

In order to estimate the SOP image background, we use the blue shaded region (see Fig.7) as a general background region. This region includes the pinhole area before the appearance of short "flashes", and the target itself before laser illumination ($t < 0$). We choose such a large region for background estimation to reduce the uncertainty of average background. For the target area after $t = 0$, we calculate the average signal and its uncertainty column-by-column (i.e. on the time basis). The background is subtracted from this time-averaged signal. After the "flash" starts to appear, the background subtraction is done in a column-by-column fashion, each column having its own background value. The signal I is then converted to temperature using $T = T_0/\ln[1 + (1 - R)A_0X(W_{S0})/\eta I]$, where T_0, A_0, X are calibration parameters, and η is the sweep rate (in pixels/ns). R is the reflectance of the Si-LiF interface for 650 nm light, and is approximated by the reflectance for 532 nm light, which in turn is extracted from the VISAR image [23].

Due to the extreme non-linearity of $T = T_0/\ln[1 + (1 - R)A_0X(W_{S0})/\eta I]$, uncertainty of temperature demands special care. A Monte Carlo routine was used to estimate the errors. Contributions include (relative) uncertainties in A_0 (3.5%), T_0 (0.2%), $X(W_{S0})$ (0.5%), R (depends on shots, usually 10-30%), and of course, I. 100,000 Monte Carlo runs are performed each shot. Due to the extreme non-linearity of this equation, the temperature distribution is generally not Gaussian. Nevertheless we define the 1-σ confidence interval by requiring $\mathrm{CDF}(T_{\mathrm{lower}}) = (1 - C)/2, \mathrm{CDF}(T_{\mathrm{upper}}) = (1 + C)/2$, where CDF is the cumulative distribution function, and $C = 68.27\%$ is the confidence level. It is found that the contribution of uncertainty of T_0, A_0, X and R to the uncertainty of T is small. It can be explained by assuming T obeys Gaussian distribution, and calculating the relative uncertainty of temperature using the following

equation:

$$\frac{\sigma_T^2}{T^2} = \frac{\sigma_{T_0}^2}{T_0^2} + \left(\frac{T}{T_0}\right)^2 \left[1 - \exp\left(-\frac{T_0}{T}\right)\right]^2 \times \left(\frac{\sigma_{A_0}^2}{A_0^2} + \frac{\sigma_X^2}{X^2} + \frac{\sigma_\eta^2}{\eta^2} + \frac{\sigma_R^2}{(1-R)^2} + \frac{\sigma_I^2}{I^2}\right) \quad (1)$$

Since T_0 is around 2 eV, and $T < 5000\,\mathrm{K}$, the pre-factor $(T/T_0)^2[1-\exp(-T_0/T)]^2 \ll 1$, therefore suppressing the terms in the last parentheses.

The Si temperature near the Si-LiF interface obtained from SOP, $T_{\mathrm{s,sop}}$, is augmented by the simulation results using the following method. We can obtain average values of bulk temperature $T_{\mathrm{b,sim}}$ and interface temperature $T_{\mathrm{s,sim}}$ during x-ray exposure from simulation. The difference between $T_{\mathrm{b,sim}}$ and $T_{\mathrm{s,sim}}$ describes the temperature non-uniformity inside the target due to complex wave interactions. Some shots (s29627 and s32082) have quite large velocity jumps ($> 2\,\mathrm{km/s}$) which could cause temperature jump. We use simulation as a reference to convert observed interface temperature to bulk temperature, $T_{\mathrm{b,sop}} = T_{\mathrm{s,sop}} - T_{\mathrm{s,sim}} + T_{\mathrm{b,sim}}$. Here we have used the property that the heat capacity of a solid is independent of temperature, at tempeartures much larger than Debye temperature.

The temperature elevation relative to the isentrope is attributed to several reasons. (1) Unavoidable small shocks, due to elastic-plastic transformation at 9 GPa [24] and a rich selection of phase transitions at low pressures. The anomaly of Hugoniot $P-V$ curve at these transitions cause wave splittings and weak shocks. (2) Impedance mismatch at the Si-LiF interface causes weak shocks. (3) Plastic work due to strength of silicon. The temperature increase due to plastic work can be written as [25]

$$\Delta T_{\mathrm{plastic}} = \frac{A m_u}{\rho_0 c_V} \int Y(\eta) \frac{\partial \varepsilon}{\partial \eta}\, \mathrm{d}\eta \quad (2)$$

where Am_u is the mass of one Si atom, c_V is the specific heat per atom and is approximated by $3k_B$, Y is yield strength, $\eta = \rho/\rho_0$ is the compression ratio, and $\epsilon = (2/3)[\ln\eta - Y/2G]$ is the plastic strain, G is the shear modulus. Y and G can be estimated by Steinberg-Guinan model [21], whose parameters can be determined using the elastic moduli results of [26].

$$\frac{Y}{Y_0} = \frac{G}{G_0} = 1 + \frac{A_0 P}{\eta^{1/3}} + B_0(T - 298.15) \quad (3)$$

$G_0 = 6.814\,\mathrm{GPa}$, $A_0 = 7.492 \times 10^{-3}\,\mathrm{GPa}^{-1}$, and $B_0 = -2.816 \times 10^{-4}\,\mathrm{K}^{-1}$. The yield strength at ambient conditions $Y_0 = 4.33\,\mathrm{GPa}$ can be found in [27]. The result is shown in Fig.6.

[1] R. Paul, S. Hu, and V. Karasiev, Anharmonic and anomalous trends in the high-pressure phase diagram of silicon, Physical Review Letters **122**, 10.1103/physrevlett.122.125701 (2019).

[2] V. N. Goncharov, T. C. Sangster, R. Betti, T. R. Boehly, M. J. Bonino, T. J. B. Collins, R. S. Craxton, J. A. Delettrez, D. H. Edgell, R. Epstein, R. K. Follett, C. J. Forrest, D. H. Froula, V. Y. Glebov, D. R. Harding, R. J. Henchen, S. X. Hu, I. V. Igumenshchev, R. Janezic, J. H. Kelly, T. J. Kessler, T. Z. Kosc, S. J. Loucks, J. A. Marozas, F. J. Marshall, A. V. Maximov, R. L. McCrory, P. W. McKenty, D. D. Meyerhofer, D. T. Michel, J. F. Myatt, R. Nora, P. B. Radha, S. P. Regan, W. Seka, W. T. Shmayda, R. W. Short, A. Shvydky, S. Skupsky, C. Stoeckl, B. Yaakobi, J. A. Frenje, M. Gatu-Johnson, R. D. Petrasso, and D. T. Casey, Improving the hot-spot pressure and demonstrating ignition hydrodynamic equivalence in cryogenic deuterium–tritium implosions on OMEGA, Physics of Plasmas **21**, 056315 (2014).

[3] M. N. Pavlovskii, Formation of metallic modifications of germanium and silicon under conditions of shock compression, Fiz. Tverd. Tela **9**, 3192 (1967).

[4] W. H. Gust and E. B. Royce, Axial yield strengths and two successive phase transition stresses for crystalline silicon, Journal of Applied Physics **42**, 1897 (1971).

[5] T. Goto, T. Sato, and Y. Syono, Reduction of shear strength and phase-transition in shock-loaded silicon, Japanese Journal of Applied Physics **21**, L369 (1982).

[6] S. J. Turneaure, S. M. Sharma, and Y. Gupta, Nanosecond melting and recrystallization in shock-compressed silicon, Physical Review Letters **121**, 10.1103/physrevlett.121.135701 (2018).

[7] E. E. McBride, A. Krygier, A. Ehnes, E. Galtier, M. Harmand, Z. Konôpková, H. J. Lee, H.-P. Liermann, B. Nagler, A. Pelka, M. Rödel, A. Schropp, R. F. Smith, C. Spindloe, D. Swift, F. Tavella, S. Toleikis, T. Tschentscher, J. S. Wark, and A. Higginbotham, Phase transition lowering in dynamically compressed silicon, Nature Physics **15**, 89 (2018).

[8] C. Li, C. Wang, J. Han, L. Yan, B. Deng, and X. Liu, A comprehensive study of the high-pressure–temperature phase diagram of silicon, Journal of Materials Science **53**, 7475 (2018).

[9] J. R. Rygg, J. H. Eggert, A. E. Lazicki, F. Coppari, J. A. Hawreliak, D. G. Hicks, R. F. Smith, C. M. Sorce, T. M. Uphaus, B. Yaakobi, and G. W. Collins, Powder diffraction from solids in the terapascal regime, Review of Scientific Instruments **83**, 113904 (2012).

[10] D. Polsin, D. Fratanduono, J. Rygg, A. Lazicki, R. Smith, J. Eggert, M. Gregor, B. Henderson, J. Delettrez, R. Kraus, P. Celliers, F. Coppari, D. Swift, C. McCoy, C. Seagle, J.-P. Davis, S. Burns, G. Collins, and T. Boehly, Measurement of body-centered-cubic aluminum at 475 GPa, Physical Review Letters **119**, 10.1103/physrevlett.119.175702 (2017).

[11] A. Lazicki, J. Rygg, F. Coppari, R. Smith, D. Fratanduono, R. Kraus, G. Collins, R. Briggs, D. Braun, D. Swift, and J. Eggert, X-ray diffraction of solid tin to 1.2 TPa, Physical Review Letters **115**, 10.1103/physrevlett.115.075502 (2015).

[12] F. Coppari, R. F. Smith, D. B. Thorn, J. R. Rygg, D. A. Liedahl, R. G. Kraus, A. Lazicki, M. Millot, and J. H. Eggert, Optimized x-ray sources for x-ray diffraction measurements at the omega laser facility, Review of Scientific Instruments **90**, 125113 (2019).

[13] S. D. Rothman and J. Maw, Characteristics analysis of isentropic compression experiments (ICE), Journal de Physique IV (Proceedings) **134**, 745 (2006).

[14] P. M. Celliers, D. K. Bradley, G. W. Collins, D. G. Hicks, T. R. Boehly, and W. J. Armstrong, Line-imaging velocimeter for shock diagnostics at the OMEGA laser facility, Review of Scientific Instruments **75**, 4916 (2004).

[15] L. E. Kirsch, S. J. Ali, D. E. Fratanduono, R. G. Kraus, D. G. Braun, A. Fernandez-Pañella, R. F. Smith, J. M. McNaney, and J. H. Eggert, Refractive index of lithium fluoride to 900 gigapascal and implications for dynamic equation of state measurements, Journal of Applied Physics **125**, 175901 (2019).

[16] D. E. Fratanduono, R. F. Smith, D. G. Braun, J. R. Patterson, R. G. Kraus, T. S. Perry, A. Arsenlis, G. W. Collins, and J. H. Eggert, The effect of nearly steady shock waves in ramp compression experiments, Journal of Applied Physics **117**, 245903 (2015).

[17] H. Olijnyk, S. Sikka, and W. Holzapfel, Structural phase transitions in si and ge under pressures up to 50 GPa, Physics Letters A **103**, 137 (1984).

[18] S. J. Duclos, Y. K. Vohra, and A. L. Ruoff, Experimental study of the crystal stability and equation of state of si to 248 GPa, Physical Review B **41**, 12021 (1990).

[19] M. Hanfland, U. Schwarz, K. Syassen, and K. Takemura, Crystal structure of the high-pressure phase silicon VI, Physical Review Letters **82**, 1197 (1999).

[20] S. Anzellini, M. T. Wharmby, F. Miozzi, A. Kleppe, D. Daisenberger, and H. Wilhelm, Quasi-hydrostatic equation of state of silicon up to 1 megabar at ambient temperature, Scientific Reports **9**, 10.1038/s41598-019-51931-1 (2019).

[21] D. J. Steinberg, S. G. Cochran, and M. W. Guinan, A constitutive model for metals applicable at high-strain rate, Journal of Applied Physics **51**, 1498 (1980).

[22] D. Orlikowski, A. A. Correa, E. Schwegler, J. E. Klepeis, M. Elert, M. D. Furnish, R. Chau, N. Holmes, and J. Nguyen, A STEINBERG-GUINAN MODEL FOR HIGH-PRESSURE CARBON: DIAMOND PHASE (AIP, 2008).

[23] M. C. Gregor, R. Boni, A. Sorce, J. Kendrick, C. A. McCoy, D. N. Polsin, T. R. Boehly, P. M. Celliers, G. W. Collins, D. E. Fratanduono, J. H. Eggert, and M. Millot, Absolute calibration of the OMEGA streaked optical pyrometer for temperature measurements of compressed materials, Review of Scientific Instruments **87**, 114903 (2016).

[24] S. J. Turneaure and Y. M. Gupta, Inelastic deformation and phase transformation of shock compressed silicon single crystals, Applied Physics Letters **91**, 201913 (2007).

[25] Y. Ping, F. Coppari, D. G. Hicks, B. Yaakobi, D. E. Fratanduono, S. Hamel, J. H. Eggert, J. R. Rygg, R. F. Smith, D. C. Swift, D. G. Braun, T. R. Boehly, and G. W. Collins, Solid iron compressed up to 560 GPa, Physical Review Letters **111**, 10.1103/physrevlett.111.065501 (2013).

[26] H. J. McSkimin and P. Andreatch, Elastic moduli of silicon vs hydrostatic pressure at 25.0°c and - 195.8°c, Journal of Applied Physics **35**, 2161 (1964).

[27] A. L. Ruoff, On the yield strength of diamond, Journal of Applied Physics **50**, 3354 (1979).

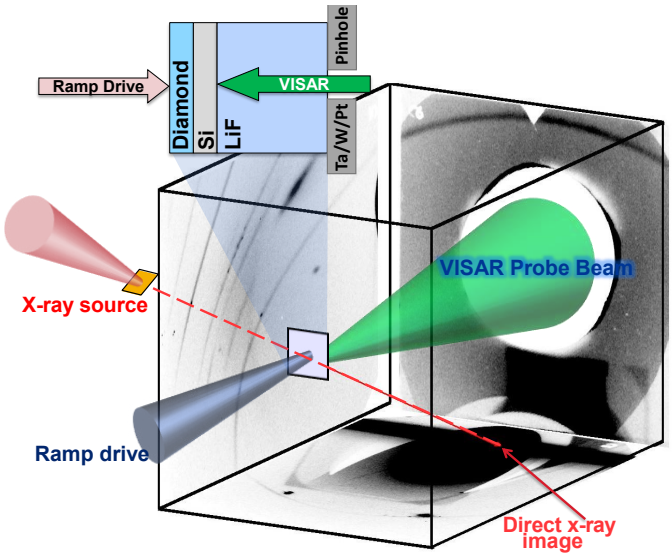

FIG. 1: The experimental configuration for x-ray diffraction of ramp-compressed materials. The target consists of either diamond ablator, silicon sample, and lithium fluoride window, or diamond ablator, copper or gold heat shield, diamond pusher, silicon sample and diamond window, bonded together in that order. The target is mounted on the front plate of the PXRDIP box and compressed by laser ablation. During peak compression, a metallic foil is illuminated by another laser beam to generate x-ray, which diffracts from the target and is recorded by the image plates inside the PXRDIP box. On the back plate is an opening allowing the VISAR probe beam to pass through.

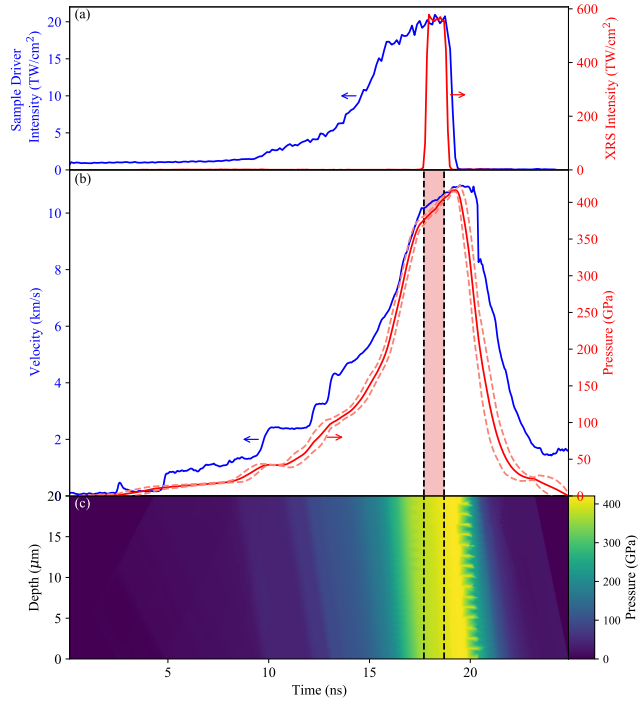

FIG. 2: An example of pressure determination for ramp compression experiments. The example shot is OMEGA EP shot 29637. (a) Ramp pulse for driving the silicon

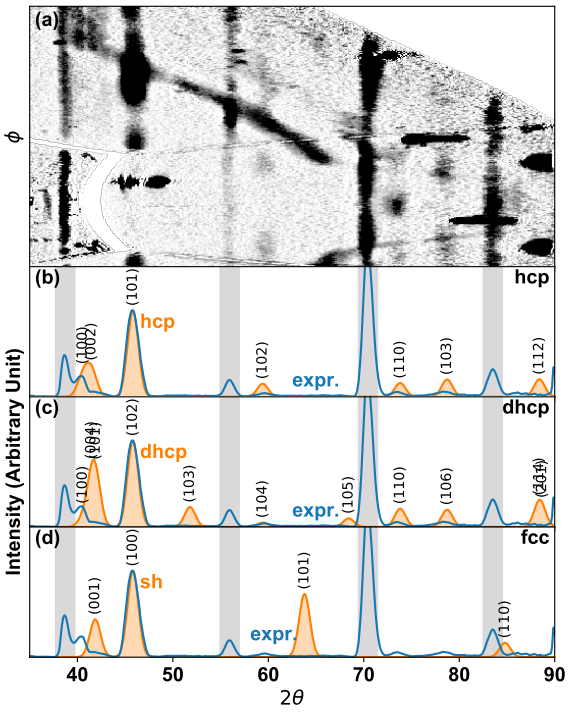

FIG. 3: Shot 32081, an example of "low pressure" shots. The pressure in the sample at the time of x-ray exposure is 48 GPa. (a) Background subtracted diffraction data in $\phi - 2\theta$ space. (cropped in ϕ direction). (b)(c)(d) The experimental x-ray intensity lineout as a function of diffraction angle 2θ (blue) is compared with simulated diffraction signal (orange) of hcp, dhcp, and sh structures. The pinhole diffraction signal is indicated by the gray shades. The rest of the peaks are from compressed Si sample. The experimental lineout matches well with hcp structure, lacks (103) peak of dhcp structure (red arrow), and does not match well with sh structure in general.

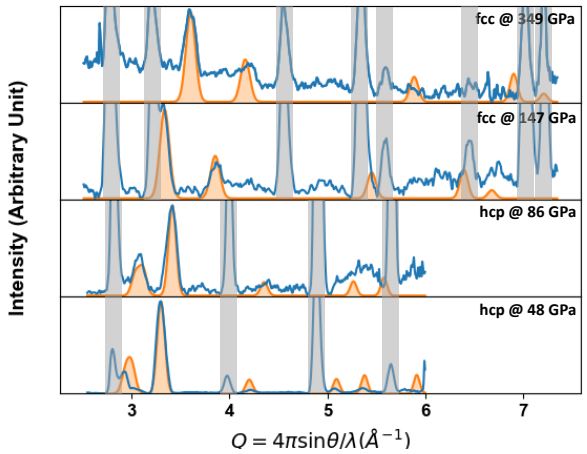

FIG. 4: Intensity lineout as a function of $Q = 4\pi \sin\theta/\lambda$ from background-subtracted $2\theta - \phi$ projections of image plates data of increasing pressure. Blue curves represents experimental lineout, while orange curve shows the simulated diffraction profile of best-fit structure and lattice parameters. Grey shaded regions represent diffraction from reference materials.

TABLE II: Shot Data Summary

Shot #	XRS	P	σ_P	Δ_P (GPa)	Phase	hkl	2θ(deg)	d(Å)	a(Å)	c/a	Density (g/cm^3)
25848	Cu	236.44	6.43	3.34	fcc	(111)	48.351	1.809(18)	3.13(2)		6.07(13)
25876	Ge	220.03	6.27	6.56	fcc	(111)	38.747	1.82(2)	3.153(18)		5.95(10)
						(200)	45.162	1.0575(17)			
25879	Ge	345.53	9.59	23.13	fcc	(111)	40.546	1.75(2)	3.013(16)		6.82(11)
						(200)	47.441	1.503(15)			
25908	Ge	152.4	5.47	14.33	fcc	(111)	37.317	1.89(2)	3.256(19)		5.40(10)
						(200)	43.78	1.622(18)			
29627	Cu	184.74	4.67	12.26	fcc	(111)	47.162	1.852(19)	3.21(2)		5.66(12)
29637	Cu	389.89	10.56	9.85	fcc	(111)	51.19	1.715(16)	2.969(12)		7.13(9)
						(200)	59.886	1.484(11)			
32082	Ge	300.44	10.09	13.31	fcc	(111)	39.883	1.77(2)	3.074(17)		6.42(11)
						(200)	46.294	1.538(16)			
29625	Cu	99.45	4.25	9.94	hcp	(100)	42.272	2.05(2)	2.369(6)	1.698(10)	4.77(5)
						(002)	43.064	2.02(2)			
						(101)	47.423	1.842(18)			
						(102)	62.379	1.430(10)			
						(110)	77.484	1.184(7)			
30135	Cu	33.02	3.15	14.29	hcp	(100)	40.236	2.15(3)	2.487(11)	1.677(13)	4.17(7)
						(002)	41.623	2.08(2)			
						(101)	45.55	1.91(2)			
32081	Cu	51.5	3.67	5.24	hcp	(100)	40.269	2.15(3)	2.473(5)	1.699(7)	4.19(3)
						(002)	40.898	2.12(2)			
						(101)	45.798	1.90(2)			
						(102)	59.618	1.490(11)			
						(110)	73.489	1.238(7)			
						(103)	78.394	1.172(6)			

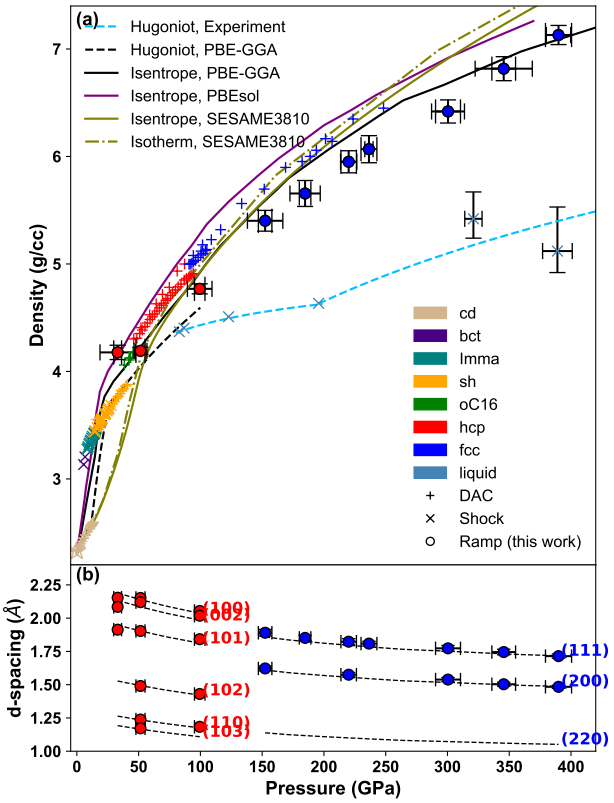

FIG. 5: (a) Density-pressure phase diagram of silicon. Static-compressed (diamond) [17][18][19], shock-compressed (square) [3][7] and ramp-compressed (circle) states are compared with theoretically calculated isentrope (with three different exchange-correlation functionals: PBE-GGA, SCAN-L, and PBEsol) and hugoniot (PBE-GGA). Pressure errorbar with small capsize represents the uncertainty of average pressure, while errorbar with large capsize represents the non-uniformity of pressure distribution inside the sample during the x-ray exposure. (b) d-spacing of lattice planes as a function of pressure. The solid curves are based on DFT calculation using PBE-GGA xc functional. The curve in the hcp portion is calculated assuming the c/a ratio is the ideal value.

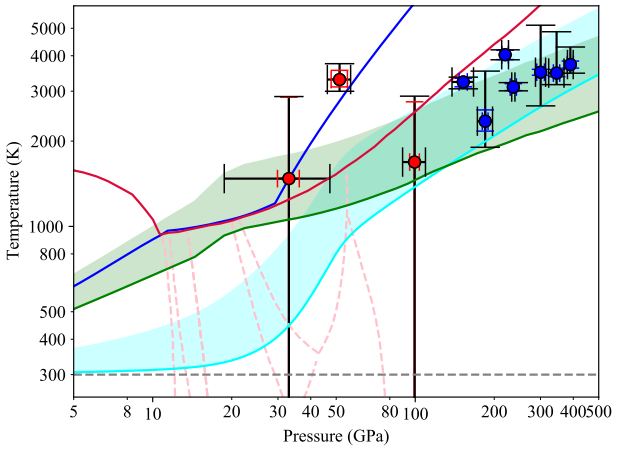

FIG. 6: T-P phase diagram of Si.

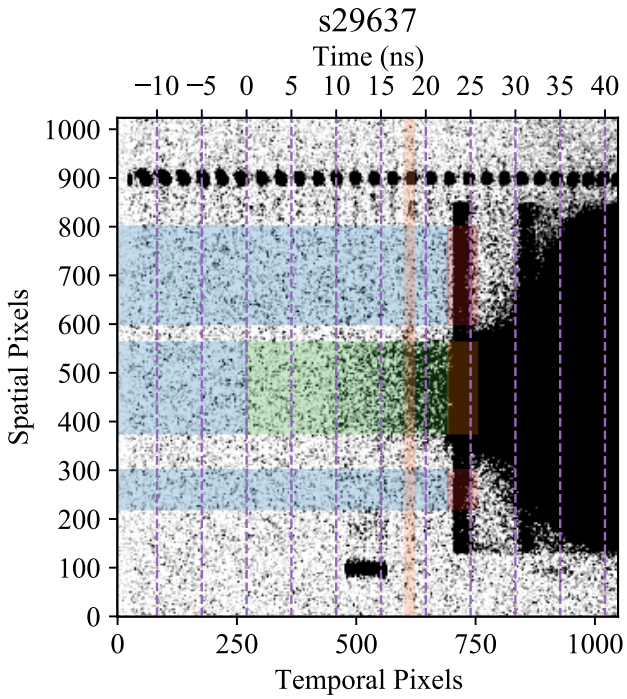

FIG. 7

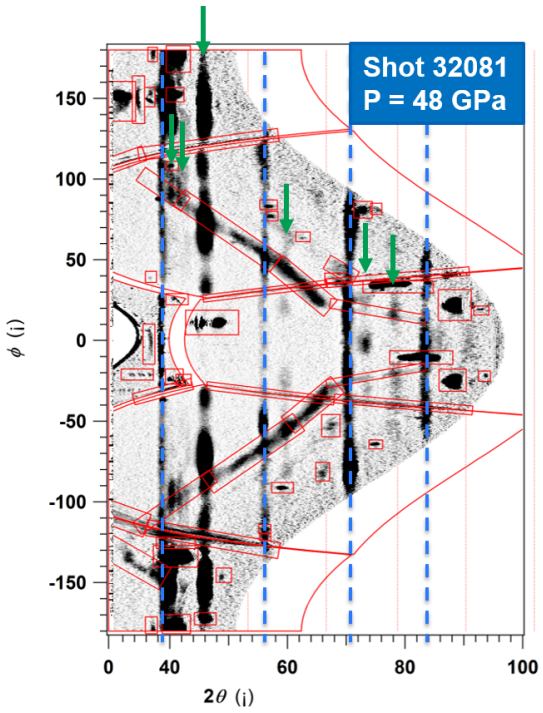

(a) s32081. P = 48 GPa.

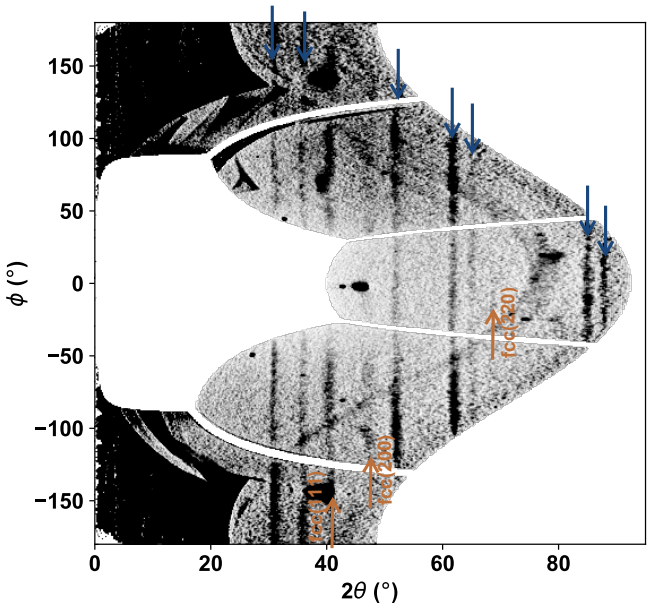

(b) s25879. P = 349 GPa.

FIG. 8: Background subtracted image plate in $2\theta - \phi$ space. (a) OMEGA EP shot 32081 at 48 GPa. (b) OMEGA EP shot 25879 at 349 GPa. The blue arrows indicate reference calibration diffraction lines. The orange arrows indicate the sample diffraction lines which are labeled by their Miller indices.